Efficient low-fidelity aeroacoustic permanence calculation of propellers

Fuerkaiti, Yunusi; Grande, Edoardo; Casalino, Damiano; Avallone, Francesco; Ragni, Daniele

Important note
To cite this publication, please use the final published version (if applicable).
Please check the document version above.

Contents lists available at ScienceDirect

Aerospace Science and Technology

www.elsevier.com/locate/aescte

Efficient low-fidelity aeroacoustic permanence calculation of propellers

Yunusi Fuerkaiti [*], Edoardo Grande, Damiano Casalino, Francesco Avallone, Daniele Ragni

Aerodynamics, Wind Energy, Flight Performance and Propulsion Department, Delft University of Technology, Delft 2629HS, the Netherlands

A B S T R A C T

A noise footprint prediction framework for propeller-driven aircraft which couples an aerodynamic model and several aeroacoustic models is presented in this study. The aerodynamic model is based on the blade element momentum theory, while the aeroacoustic models are based on a time-domain compact dipole/monopole Ffowcs-Williams and Hawking's acoustic analogy, a trailing edge noise model, and a noise hemisphere database approach including a straight-ray propagation model, respectively. In order to reduce the runtime, the frequency-domain acoustic formulation, derived by Hanson (1980), is implemented and validated against the compact dipole/monopole Ffowcs-Williams and Hawking's acoustic analogy. The framework evaluates the acoustic effects of variations in the design and operating conditions of a propeller in forward flight. Noise footprints, obtained with different propeller configurations having varying advance ratio and number of blades are compared. It is found that, for a given thrust, a drop in advance ratio alters the source directivity dramatically, which resulting in a variation of up to 30 dBA on the acoustic footprint. When the advance ratio is kept the same and the number of blades increases from 5 to 7, the variation becomes 16 dBA due to the change in the source directivity, but the maximum noise level remains the same. The latter condition reduces the loading for each blade, and consequently the associated noise. However, the total noise remains unchanged as a consequence of increasing thickness noise due to the lower advance ratio, high blade tip Mach number, and addition of extra blades.

1. Introduction

Aircraft noise is the most significant source of adverse community reaction related to the operation and expansion of airports. Aircraft noise has often been cited as the most undesired noise in the urban community because of its adverse impacts on health, including annoyance [1], sleep disturbance [2,3], cardiovascular diseases [4] and altered cognitive performance among children [5]. However, this is expected, particularly for Urban Air Mobility (UAM) operations, to remain the case in most regions of the world for the foreseeable future.

UAM vehicles, as electric Vertical Takeoff and Landing (eVTOL) vehicles, are expected to operate with zero operational emissions and at a lower noise level due to the removal of combustion engines compared to conventional aircraft. Propellers constitute the most employed propulsive system for this kind of vehicles since they guarantee high efficiency for low flight speed; they can be placed, sized, and operated with greater flexibility to leverage the synergistic benefits of aero-propulsive coupling and provide im-

proved performance over traditional aircraft [6]. As such, the eVTOL operations are governed by strong variations in flight speed, propeller tilt angles, altitude, gross weight, and specific vehicle configuration. These variations are reflected on the noise footprint throughout the mission time.

Since eVTOL vehicles are still under development, and the community's opinion on these vehicles is still forming, limiting the noise impact on the community at an early stage is crucial. Noise-Power-Distance (NPD) data [7], which are specific to each aircraft, have been widely used to evaluate aircraft noise footprint. However, NPD data can not be applied for eVTOL vehicles as they differ in many ways from conventional aircraft. In the absence of NPD, most of the approaches adopted to evaluate aircraft noise for different flight trajectories and operating conditions start from sampling noise sources over a hemisphere surrounding the aircraft [8–11]. The noise sources are then propagated on the ground either using the straight-ray propagation model with the assumption of constant weather conditions or using the curved-ray propagation model [10] that accounts for the sound wave refraction due to the wind and temperature gradients. The weather has a significant impact on long-range propagation, but it plays a small role in short-range propagation distances over a flat terrain [10]. The present work focuses only on the acoustic impacts of source pa-

rameters on the noise emission and footprint of a propeller; thus, the effect of weather conditions is beyond the scope of this work.

The aforementioned studies used either high-fidelity CFD simulation or experimental measurement data to compute noise hemispheres associated with different operating conditions. Furthermore, high-fidelity CFD simulations have been directly used to predict aircraft noise emission from the component level [12–14] to full vehicle configuration restricted to relatively low-frequency problems [15–18]. Since both high-fidelity CFD simulation and experimental measurement are too expensive for the design and evaluation of low noise aircraft and flight mission profiles that are typically involved in evaluations of hundreds of noise hemispheres, they cannot be coupled with a design optimization process to explore acoustic effects of the design and operating parameters on the noise footprints in an industrial context.

Low-fidelity methods, such as Blade Element Momentum Theory (BEMT), have been widely used for the calculation of the steady loading of propellers, and they can also be coupled with an acoustic module to retrieve the tonal acoustic radiation [19–22]. Pascioni et al. [22] evaluated the noise footprint of a distributed propulsion aerial vehicle using low-fidelity methods and a straight-ray propagation model. Only tonal noise was considered, and an attempt was made to explore the acoustic effect of varying phase angle on the acoustic footprint in a small square area (50 m by 50 m). However, assessments of low noise aircraft and flight mission profiles necessitate the evaluation of aircraft noise footprints over large square areas and at different time-instance along the flight mission time. In addition, broadband noise will be much more critical for UAM vehicles than for conventional aircraft as UAM vehicles are expected to operate at lower tip speeds [23]. This paper considers only the propeller trailing edge noise. Bian et al. [24] investigated UAM and drone noise impact on the environment using a low-fidelity approach and Gaussian beam propagation model. Noise sources were modeled using aerodynamic variables [25] instead of considering blade geometry and load distributions along a blade span.

Kotwitcz et al. [26] examined the accuracy of several acoustic frequency methods coupled with the BEMT across a range of propeller geometries and operational conditions. They found out that any aerodynamic error introduced by the BEMT has a negligible impact on the acoustic solution and highlighted the efficiency and reliability of early acoustic methods such as Hanson's helicoidal surface model [27] for propeller tonal noise prediction. Casalino et al. [28] established a benchmark activity for propeller aeroacoustics based on a small unmanned aerial vehicle (UAV) through comparisons between experiments, high-fidelity simulations based on the Lattice Boltzmann Very Large Eddy Simulation (LB/VLES) method, and low-fidelity computations. For the latter, a BEMT method is used for the loads predictions, coupled with a compact dipole/monopole Ffwocs-Williams and Hawkings (FW-H) acoustic analogy formulation for tonal noise predictions and a trailing edge noise module. Accurate forces and tonal noise prediction were achieved using the low-fidelity workflow. Nevertheless, these studies focused on the radiated noise from stationary sources and short propagation distances a few times larger than the rotor diameter. Source motion, acoustic footprints over a large square area, and the noise impact on the community were not considered.

Recently, Poggi et al. [29] proposed surrogate models for predicting propeller aerodynamics and noise emission based on Artificial Neural Networks (ANN). A three-bladed single propeller was considered, and acoustic impacts of varying blade twist and chord distributions were evaluated. Accurate aerodynamic and aeroacoustic predictions were achieved within the outlined boundaries of training data. However, as highlighted by authors [30,31], one of the crucial limitations of surrogate models based on ANN is their

inability to generalize outside of their training distribution, i.e., the inability to extrapolate a solution when the input falls outside the training space. They can provide very accurate results that can be comparable to the high-fidelity simulation results (of course, if the training data are provided by high-fidelity simulation).

This paper presents a computationally efficient and robust methodology to investigate the acoustic impact of design and operating parameters on the noise footprint of an isolated propeller in forward flight. To this purpose, the low-fidelity simulation workflow developed by Casalino et al. [28] and described above is extended to compute the noise footprint of a propeller. The research focused on the fast evaluation of acoustic effects of propeller advance ratio and blade count, which are the main driven factors that directly affect the noise footprint of an aerial vehicle. The presented methodology is not restricted to a specific propeller type or a flight condition. Instead, it can be applied to any propeller-driven aerial vehicle for noise emission and footprint predictions as well as flight mission analysis.

The remainder of this paper is structured as follows. In section 2, the low-fidelity workflow is described. In section 3, the propeller geometry and the validation of the low-fidelity workflow against high-fidelity simulation are presented. In section 4, a parametric study to investigate the acoustic effects of varying numbers of blades and advance ratio on the acoustic footprint of the propeller is carried out. Finally, the conclusions of the work are given in section 5.

2. Overview of the low-fidelity approach

A standard hybrid approach is used to predict the source noise levels as well as the noise footprint of an isolated propeller. Once the propeller geometry is given in terms of blade and hub geometry, BEMT computations are carried out by means of the $Opty\partial B$-BEMT tool to compute the radial distribution of aerodynamic loads and integral boundary layer parameters that represent the input for the tonal and broadband aeroacoustic predictions, respectively. Subsequently, the noise signals on microphones distributed on a hemisphere surrounding the propeller are computed using the $Opty\partial B$-PNOISE tool. Finally, the propeller noise footprint is computed using the Noise Hemisphere Database (NHD) approach implemented in $Opty\partial B$-FOOTPRINT with a straight-ray propagation model. A schematic illustration of the computational framework is displayed in Fig. 1.

2.1. Source noise prediction

The $Opty\partial B$-BEMT and $Opty\partial B$-PNOISE tools constitute the source noise prediction part. $Opty\partial B$-BEMT adopts a conventional BEMT formulation with uniform inflow and Prandtl tip-loss correction for the loads prediction. The aerodynamic module implemented inside the tool is based on the coupled panel/boundary layer model by Drela & Giles [32]. Details of the formulation can be found in the work of Casalino et al. [28]. The $Opty\partial B$-PNOISE tool is used to predict the source noise levels in which the tonal noise contribution is computed using the time-domain FW-H formulation based on the compact dipole/monopole formulation by Casalino et al. [15] and the broadband noise contribution is predicted using the trailing edge noise model by Roger and Moreau extended to a rotating blade and by using the Schinkler and Amiet WPS model [15].

2.2. NHD-based noise footprint prediction

As mentioned above, the $Opty\partial B$-FOOTPRINT is used to compute the noise footprint of an isolated propeller. The user can input a series of waypoints defining the vehicle's planned trajectory
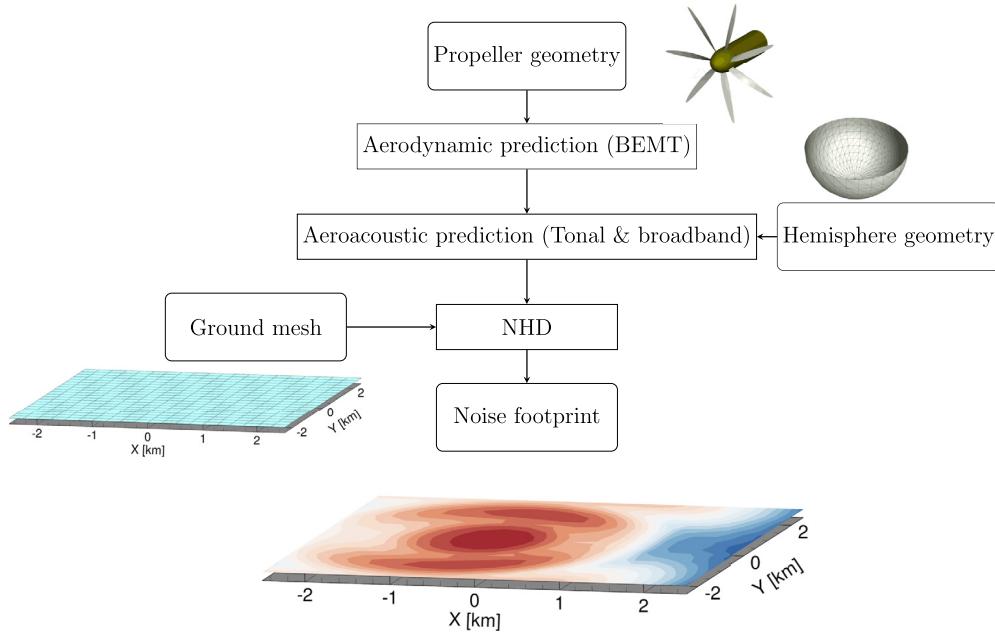
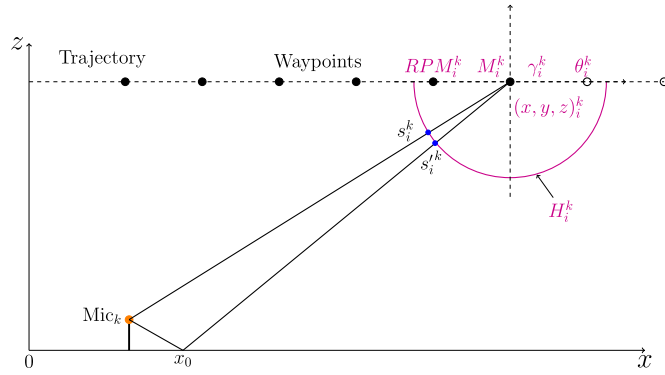**Fig. 1.** A schematic illustration of the computational framework.

Fig. 2. Illustration of the straight-ray NHD-based noise footprint calculation procedure.

that represents a portion of or a complete flight mission profile. The model subdivides this trajectory into a number of steady-state flight segments, each of which is then associated with a noise hemisphere representing the frequency and magnitude of noise radiated by the propeller over a range of directions for that particular steady flight condition. For each noise hemisphere, $Opty\partial B$-BEMT and $Opty\partial B$-PNOISE are subsequently run to compute the noise signals on the microphones distributed on it. Finally, the noise footprint of the propeller is predicted using the straight-ray propagation model with the assumption of constant weather condition.

In this study, a single flight condition that represents a constant speed level flight with constant flight direction is considered. As shown in Fig. 2, for every microphone k on a ground surface and for every time window i of 0.5 s duration, the emission time position of the vehicle along its trajectory is determined. At this position, the glide angle γ_i^k and the Mach number M_i^k are calculated from the coordinates of the trajectory waypoints, whereas the pitch angle θ_i^k, the rotor RPM_i^k are interpolated from the closest waypoints. Afterward, the angle of attack α is estimated by subtracting the pitch angle from the glide angle ($\alpha_i^k = \theta_i^k - \gamma_i^k$). Then, the narrow-band noise levels are interpolated at s_i^k and $s_i'^k$ from the closest points on the hemisphere. Finally, the ground noise levels are calculated using the direct and reflected ray paths, atmo-

spheric absorption according to the standard procedure SAE ARP 866A, Doppler shift, and amplitude corrections.

3. Low-fidelity approach validation

The $Opty\partial B$-BEMT and $Opty\partial B$-PNOISE tools were assessed in the previous work from Casalino et al. [28] by comparing against experimental measurements and high-fidelity simulations from a small UAV propeller. In this study, the low-fidelity approach is validated with high-fidelity simulations conducted using the high-fidelity CFD solver SIMULIA PowerFLOW® based on the LB/VLES method coupled with FW-H acoustic analogy [33] (referred to as high-fidelity approach hereafter). Afterwards, the validity of the frequency-domain acoustic formulation [27] is verified by comparing it against the time-domain compact dipole/monopole formulation as well as high-fidelity simulation results. Finally, the validity of the outlined numerical approach is verified by comparing the noise footprints computed with the low-fidelity approach and the high-fidelity approach.

The source noise in the high-fidelity approach is predicted by employing the FW-H solver of SIMULIA PowerACOUSTICS® on the scale-resolved flow data from PowerFLOW®. The FW-H solver is based on a forward-time solution [34] of Farassat's formulation 1A [35]. For this purpose, multiple permeable surfaces, constituted by cylinders encapsulating the propeller (see Fig. 4), are used to collect the fluctuations of the flow quantities, thus including the non-linear contribution of quadruple surfaces in the volume of fluid around the propeller, which are neglected in the low-fidelity approach. The signals on the cylinders are averaged to filter out spurious noise introduced by the larger vortical structures from the wake of the propeller. Broadband noise is also predicted, due to the scale-resolving property of the LB/VLES model. Casalino et al. [28] performed a grid convergence study using the 3DS aeroacoustic workflow. A range of grid resolutions that spans from coarse to fine was used and the grid convergence was verified by monitoring the force and tonal noise with a medium resolution. In this work, the same medium resolution within the same workflow is employed to generate the high-fidelity simulation results, instead of repeating the grid convergence study.

(a)

(b)
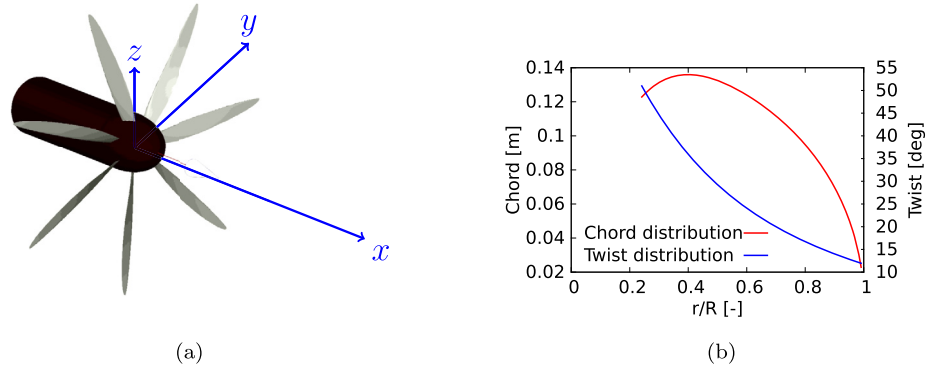
Fig. 3. Propeller geometry and the reference system (a). Propeller chord and twist distributions (b). (For interpretation of the colors in the figure(s), the reader is referred to the web version of this article.)

(a)

(b)
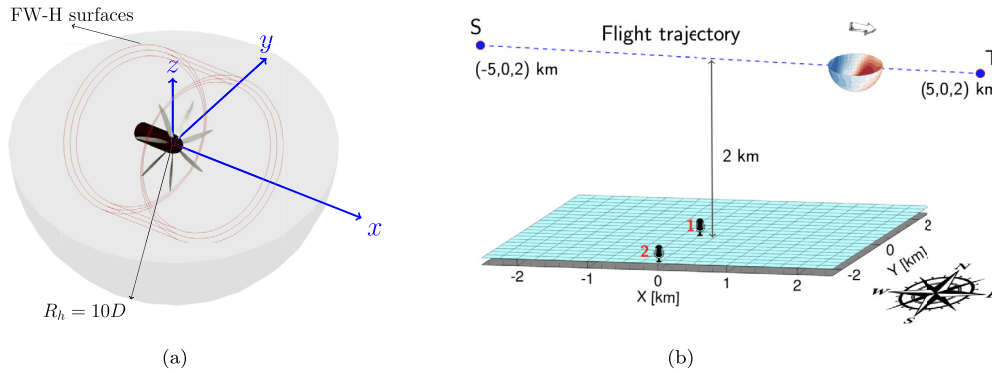
Fig. 4. Propeller model of the reference case, including the permeable sampling surfaces for FW-H acoustic propagation and the noise hemisphere (a). The geometry of the problem (b).

Table 1
Specifications and operational conditions of the reference case.

Flight Mach Number (M)	0.2	-
Rotational Speed	1900	RPM
Total thrust (T_h)	1500	N
Advance Ratio (J)	0.84	-
Diameter (D)	2.5	m
Blade Number (NB)	7	-
Hub-to-Tip Ratio	0.1064	-
Flight Altitude	2000	m

3.1. Case setup

The propeller geometry together with the employed reference system is shown in Fig. 3a. The chord and twist radial distribution are plotted in Fig. 3b. The propeller is cruising at a 2 km altitude. The propeller geometrical specifications and operating conditions of the reference case are listed in Table 1. The noise hemisphere is defined in the propeller reference system (zero pitch, yaw, and roll). The hemisphere radius R_h is set to 10 times the propeller diameter D to ensure the flow pressure is fully recovered and only acoustic pressure exists. The hemisphere is discretized in 17 parallels and 17 meridians. The hemisphere and propeller geometry along with the FW-H surfaces for the reference case are shown in Fig. 4a.

For the noise footprint, a straight-level flight trajectory is considered, as illustrated in Fig. 4b. The flight trajectory starts at the starting point S (-5, 0, 2) km and terminates at terminal point T (5, 0, 2) km. The flight direction points to the positive x-axis. An unperturbed atmosphere is used as the domain of the computa-

tion, where no wind and no temperature gradients are present. The model outputs the A-weighted OASPL for two prescribed microphones as well as microphones located in a 5 km square area discretized by 21 by 21 grid points on a hard ground plane. The first microphone (Mic 1) is located at the center of the ground plane (0, 0, 3) m and the second microphone (Mic 2) is located at (0, -2500, 3) m as indicated in Fig. 4b.

3.2. Aerodynamic validation

For the given rotational speed of 1900 RPM, the aerodynamic forces acting on the propeller blades are balanced iteratively through varying the collective pitch angle in order to generate the required target thrust of 1500 N. This is accomplished by means of an automatic trimming procedure integrated into the high-fidelity workflow. The reference collective pitch angle and the thrust obtained are -8.1° and 1520 N, respectively. The reference collective pitch angle is then given as an input along with the propeller geometry into *Opty∂B*-BEMT tool. The total thrust predicted with the *Opty∂B*-BEMT tool is 1517.06 N and it is in very good agreement with the reference one and the error between the two is 0.19%.

Fig. 5 represents the sectional thrust dT/dr and thrust coefficient C_T distributions along the blade radial direction. The sectional thrust distribution from the low-fidelity method (indicated as LF) is slightly underpredicted at $r/R <= 0.43$ and $r/R >= 0.78$ and overpredicted between $r/R = 0.45$ and $r/R = 0.74$ with respect to the high-fidelity prediction (indicated as HF). The underprediction is likely due to the limitations of the root and tip loss correction models that are implemented in the *Opty∂B*-BEMT tool. Overall, the low-fidelity simulation results show a favorable agreement with the high-fidelity simulation results.
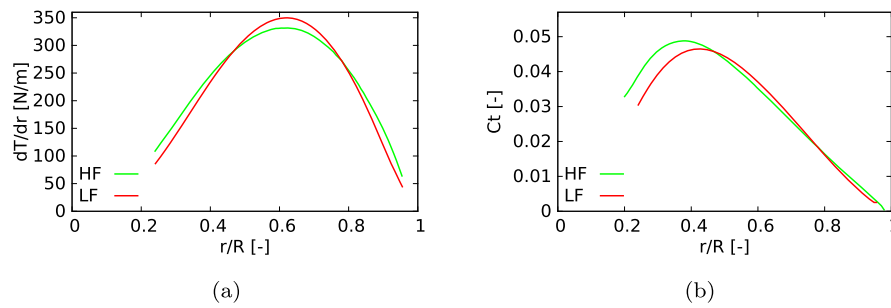
Fig. 5. Sectional thrust distribution (a) and thrust coefficient (b) along the blade radial direction.
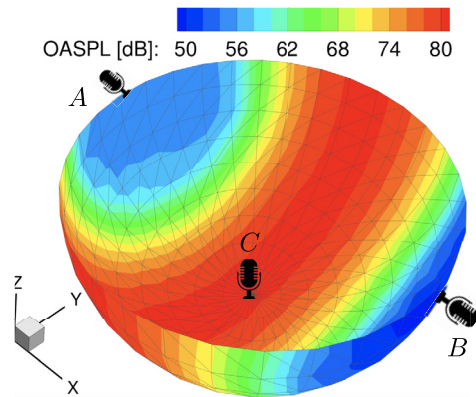

Fig. 6. Overall Sound Pressure Levels (OASPL) over the noise hemisphere computed with the high-fidelity approach.

3.3. Aeroacoustic validation

In this section, the validity of the time-domain compact dipole/monopole formulation as well as the trailing edge noise model implemented in $Opty\partial B$-PNOISE is checked by comparing against the high-fidelity simulation results. Furthermore, the frequency-domain acoustic formulation derived by Hanson [27] (indicated as FD) is compared with both high-fidelity and $Opty\partial B$-PNOISE results. The frequency-domain formulation is implemented in an in-house code based on the revised formulations given in [26]. It outputs only the tonal noise component based on the blade geometry and forces distribution along the blade span obtained with the $Opty\partial B$-BEMT tool, while the low-fidelity approach outputs both tonal and broadband noise. The OASPL on the hemisphere computed with the high-fidelity approach within a band from 200 Hz to 240 Hz that encompasses only the first Blade Passing Frequency (BPF) 221.67 Hz is shown in Fig. 6. Broadband contribution on the hemisphere is compared at microphone locations A $(-10D, 0, 0)$ m, and B $(10D, 0, 0)$ m, while the tonal contribution is compared at microphone location C $(0, 0, -10D)$ m. The microphone A and B are located on the propeller axis, while microphone C is located at the propeller rotation plane as indicated in Fig. 6.

The comparisons of broadband contribution at microphone A and microphone B computed with the $Opty\partial B$-PNOISE trailing edge noise module (indicated as LF) and high-fidelity predictions (indicated as HF) are displayed in Fig. 7a and Fig. 7b, respectively. As expected, the spectral content of microphone A and B, located in a plane perpendicular to the propeller plane (see Fig. 6), is mainly broadband due to turbulent boundary layer trailing edge noise. At microphone A, the low-fidelity approach overpredicts the high-fidelity result at all harmonics under consideration. It is noted that the difference between the two approaches is minimum at the first harmonic of BPF and it increases with the increasing number

of harmonics. At microphone B, the low-fidelity approach shows slightly better agreement than that of microphone A where the high-fidelity prediction decays faster at higher harmonics. A close agreement is observed at the first harmonic of BPF where the difference is 5.1 dB. These discrepancies are likely due to the limitations of the empirical trailing edge noise model that were used to compute the broadband noise.

The comparison of tonal contribution at microphone C computed with the frequency-domain formulation (indicated as FD), time-domain compact dipole/monopole formulation (indicated as TD), and high-fidelity approach is shown in Fig. 7c. The frequency-domain formulation is compared against both time-domain formulation and high-fidelity one. An excellent agreement is found between the frequency-domain and time-domain predictions at the first harmonic of BPF, while both models slightly underpredict the high-fidelity result. At higher harmonics of BPF, however, the noise levels predicted with the frequency-domain model decay faster compared to the time-domain and high-fidelity predictions. This is attributed to the general behavior of the Bessel function that decays rapidly and oscillates around zero when its argument increases considerably. Moreover, the thickness and loading noise components (indicated as T and L, respectively), due to the volume displacement in the propeller rotation plane and the steady loading on the propeller blades, respectively, are computed from the time-domain and frequency-domain models and compared against each other as shown in Fig. 7d. For the first harmonic of BPF, both loading and thickness noise components predicted with the two models are identical. From the second harmonics of BPF, the frequency domain model starts to underpredict both loading and thickness noise components, and the difference between these two models increases at higher harmonics. The difference is more noticeable in the loading noise prediction than the one in the thickness noise prediction. It is noted that, independently from the prediction model, the loading noise decays faster than the thickness noise at higher harmonics.

Fig. 8 compares the source directivity at the first harmonic of BPF at different microphone positions on the hemisphere with respect to the propeller reference system. On the xy-plane (Fig. 8a), the frequency-domain model correctly captures the trend of the time-domain prediction at the microphones around the propeller rotation plane. As noticed in Fig. 7c, both frequency-domain and time-domain models slightly underestimate the levels at the microphones on the propeller plane. The frequency-domain model predicts zero levels at the microphones close to the propeller axis, i.e. around $0°$ and $180°$, as the broadband noise dominates at those microphone locations. A good agreement is observed between the prediction models at the propeller plane. On the xz-plane (Fig. 8b), the frequency-domain model is in good agreement with both low-fidelity and high-fidelity approaches around the propeller plane. The low-fidelity prediction is in better agreement with the high-fidelity prediction around $180°$ with a maximum difference of around 3 dB than that of around $0°$ with a maximum difference
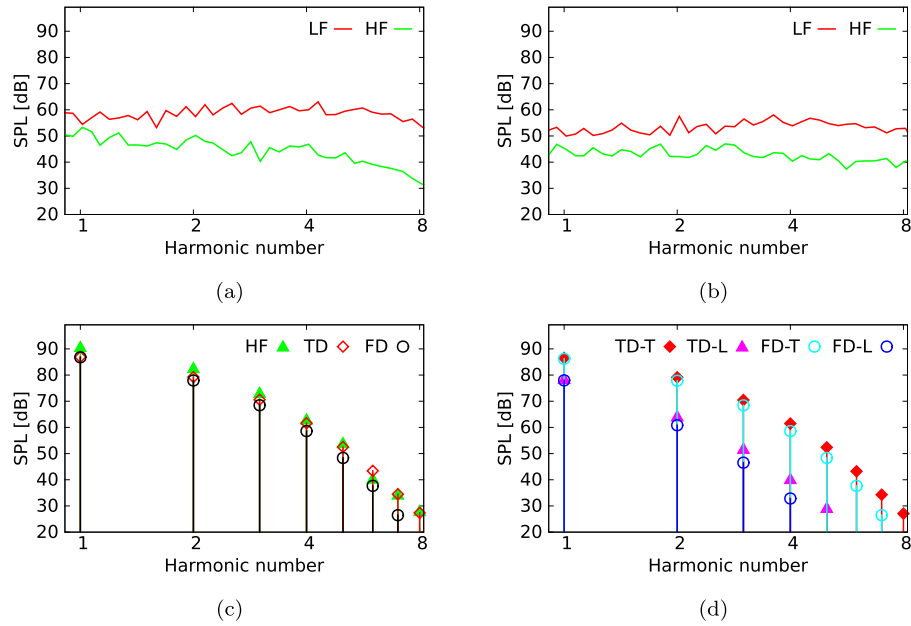
Fig. 7. Comparison of the broadband contribution predicted with high-fidelity (HF) and low-fidelity (LF) approaches at microphone *A* (a) and microphone *B* (b) on the hemisphere. Comparison of the tonal contribution predicted with high-fidelity, low-fidelity time-domain (TD), and frequency-domain (FD) formulations at microphone *C* (c). Comparison of the thickness (T) and loading (L) noise contributions at microphone *C* (d).
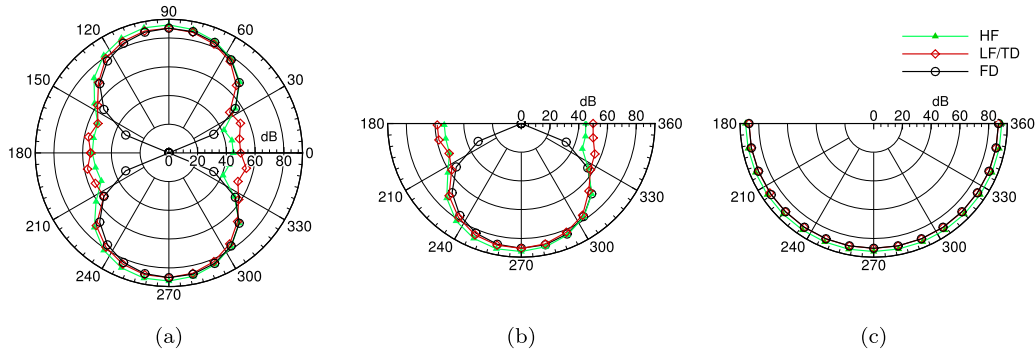
Fig. 8. Source directivity at the first BPF at xy-plane (a), xz-plane (b), and yz-plane (c).

of around 9 dB. On the yz-plane (Fig. 8c), both frequency-domain and time-domain predictions are identical. As noticed in Fig. 7c, both models slightly underpredict the high-fidelity result with a maximum difference of around 2 dB.

In general, the frequency-domain model demonstrates good agreement with the time-domain and high-fidelity results in all the three planes under consideration, suggesting that it can be readily applied for propeller tonal noise prediction, especially for design and optimization studies, where a low CPU time is desired.

The noise hemispheres computed with both high-fidelity and low-fidelity approaches are projected onto the ground using the straight-ray propagation model along with the NHD-based footprint prediction methodology. It should be noted that the noise footprint is studied within a frequency band that encompasses only the first harmonic of BPF due to the dominance of low-frequency noise in most flight conditions and its efficient propagation in the atmosphere. The noise signatures at Mic 1 and Mic 2 are overlayed in Fig. 9. At both microphone locations, the low-fidelity approach accurately predicts the trend of the high-fidelity results. Yet, there are discrepancies up to 5 dBA and 6 dBA at Mic 1 and Mic 2, respectively, that are observed in the first 30 s of the flyover time. These discrepancies are attributed to the mismatch between the two approaches that were observed at Mic *A* and Mic *B* at which the broadband noise dominates. It is noted that

the noise signature at Mic 2 shows a completely different pattern and the maximum noise level drops by 10 dBA compared to the one at Mic 1. This can be interpreted by examining the source directivity on the hemisphere at the ray-hemisphere intersection points, i.e. source emission points. Fig. 10 displays the noise footprint of the propeller at reception time 70 s, computed with both high-fidelity and low-fidelity approaches, together with the field difference between the two approaches. The interference pattern on the noise footprint is attributed to the source directivity and the emission points on the hemisphere at the emission time as well as the ground reflection. A good agreement is found between the two footprint results. The maximum difference observed is 3.5 dBA.

Overall, the close agreement between the low-fidelity and high-fidelity approaches from the source noise hemisphere to the noise footprints suggests that the low-fidelity approach is sufficient to model the tonal noise of a propeller in forward flight.

4. Acoustic effects of varying advance ratio and number of blades

In this section, the acoustic effects of varying advance ratio (*J*) and the number of blades (*NB*) on the noise footprints of the propeller are studied using the low-fidelity approach. In total 3 cases that feature the acoustic effect of varying advance ratio and the
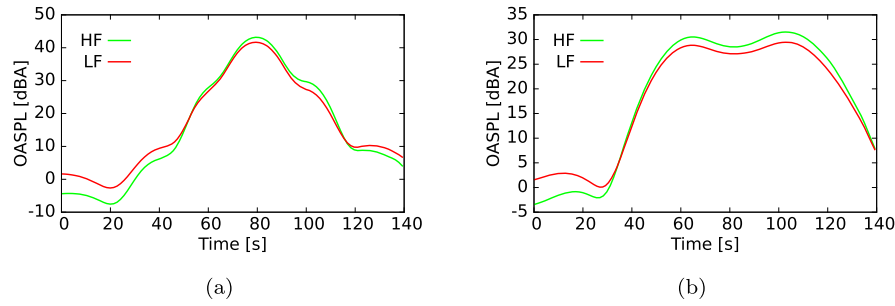
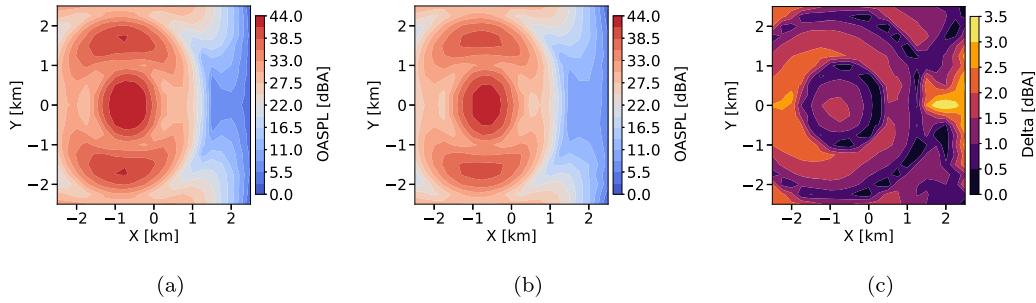**Fig. 9.** Noise signature at Mic 1 (a) and Mic 2 (b).

Fig. 10. Noise footprint at flyover time 70 s. (a) High-fidelity result. (b) Low-fidelity result. (c) Field difference between these two results.

Table 2
Test matrix for the parametric analysis.

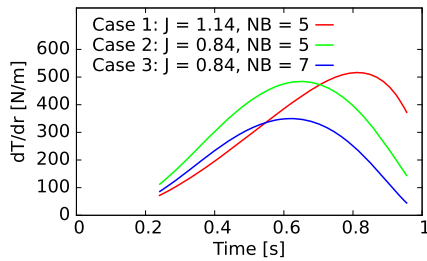| Case #	RPM	NB	J	Collective pitch angle	BPF [Hz]
1	1400	5	1.14	1.27°	116.67
2	1900	5	0.84	−7.55°	158.33
3	1900	7	0.84	−8.10°	221.67

Fig. 11. Sectional thrust distribution for a single blade.

number of blades are considered. The test matrix for this analysis is listed in Table 2. For all cases, the same blade and hub geometry as outlined in section 3 are considered; the flight altitude, Mach number, and the thrust are kept the same as 2 km, 0.2, and 1500 N, respectively. This implies that the blade is trimmed (varying the collective pitch angle) to generate the required thrust at different operating conditions. The sectional thrust distribution along a single blade span for all the test cases is displayed in Fig. 11. When the value of J decreases while the number of blades remains the same, the peak value of sectional thrust is reduced and shifted from a location around the blade tip, i.e., $r/R = 0.83$, towards the mid-span, i.e., $r/R = 0.63$. The peak value of sectional thrust decreases further when the number of blades increases and the value of J remains the same.

For all cases, the OASPL predicted over the hemisphere is calculated within a frequency range that encompasses only the first harmonic of BPF. Noise hemispheres are displayed in Fig. 12. Comparing the noise hemispheres in Case 1 and Case 2, a drop in the value of J raises the noise levels and alters the source directivity accordingly. The noise intensifies significantly around the propeller

rotation plane and spreads towards the propeller axis. The maximum OASPL on the noise hemisphere in Case 2 is increased by 10 dB and there is up to 14 dB difference on the noise hemisphere as shown in Fig. 12d, due to the variation in the source directivity, which is mainly distributed on the left lower segment of the hemisphere. Comparing the noise hemisphere in Case 2 and Case 3, an increase in the blade count changes the source directivity considerably but does not affect the maximum OASPL on the hemisphere. The maximum difference on the noise hemisphere is 8 dB that is distributed on the right lower segment of the hemisphere. Noise footprints are then studied with the prescribed ground microphones and boundary conditions described in section 3.

4.1. J variation

The acoustic impact of varying J on the noise footprint is examined by comparing Case 1 and Case 2, in which the number of blades is the same while the value of J is decreased. The source spectra at microphone C on the hemisphere (see Fig. 6) are compared and displayed in Fig. 13. When the value of J decreases, the thickness noise increases significantly at all harmonics under consideration, while an increase in loading noise is visible only at the first three harmonics. As seen, thickness noise is more sensitive in the variation of advance ratio than the loading noise. Moreover, tonal peaks after the first harmonic of BPF diminish for Case 1, while an increase in the noise levels with more evident tonal peaks is observed in Case 2, as shown in Fig. 13c. As a consequence, the OASPL on the hemisphere raises (see Fig. 12).

The corresponding noise signatures at the prescribed ground microphone locations are shown in Fig. 14. As a result of decreasing J, the noise levels at Mic 1 and Mic 2 are increased up to 13.5 dBA and 15 dBA, respectively. The interference pattern becomes more evident and the reception time of the maximum A-weighted OASPL is delayed about 10 s. The noise footprints at flyover time 70 s are compared and displayed in Fig. 15. The noise footprint in Case 2 shows totally different patterns and higher noise levels with respect to Case 1 due to the change in the source directivity and the corresponding frequency content on the hemisphere. The maximum noise level increased by 12.8 dBA and the difference be-
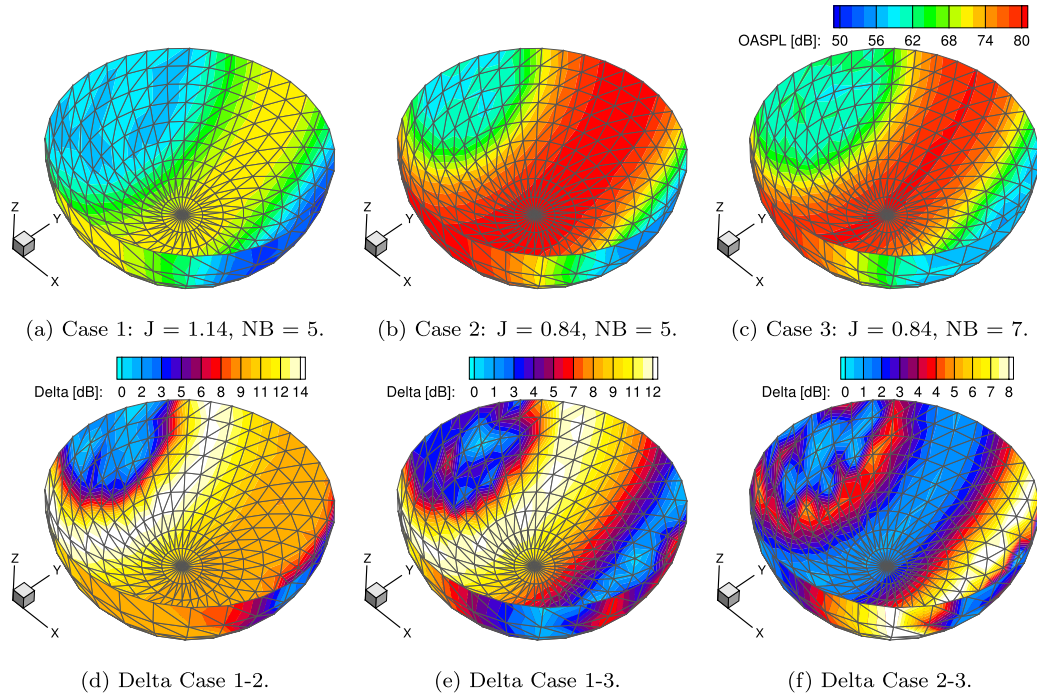
(a) Case 1: J = 1.14, NB = 5.

(b) Case 2: J = 0.84, NB = 5.

(c) Case 3: J = 0.84, NB = 7.

(d) Delta Case 1-2.

(e) Delta Case 1-3.

(f) Delta Case 2-3.

Fig. 12. Noise hemispheres and the field difference between them for the test cases under consideration.
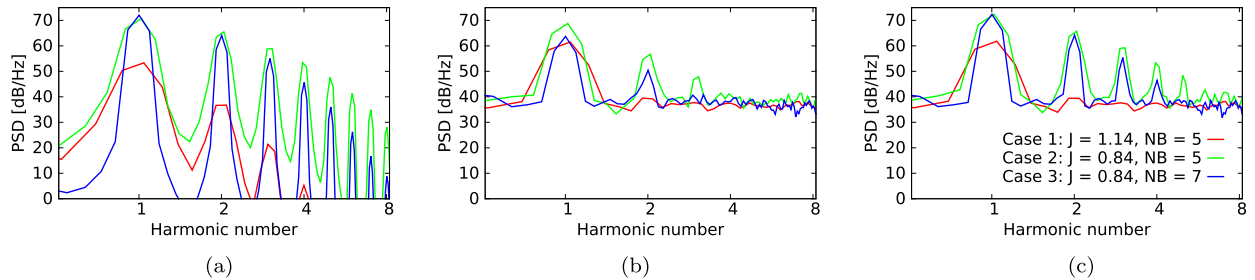

(a)

(b)

(c)

Fig. 13. Comparison of the Source spectra at microphone *C* on the hemisphere for thickness noise (a), loading noise (b), and total noise (c).

tween the footprints is 30 dBA that is mainly distributed at the left edge of the ground area.

The results presented above agree with similar studies [36,37], where they found that the on-ground noise levels increase when flight speed increases.

4.2. NB variation

The acoustic effect of varying number of blades is investigated by comparing Case 2 with Case 3. The source spectra at the microphone *C* on the noise hemisphere are compared and displayed in Fig. 13. When *NB* increases, the thickness noise at the first BPF slightly increased, and then it drops gradually with increasing number of harmonics. As expected, a clear drop in the loading noise at all harmonics is seen. Furthermore, the tonal peak due to the loading noise diminishes after the second harmonics of BPF, while it is still visible at the third harmonic in Case 2. In general, both thickness and loading noise drop considerably at higher harmonics as a consequence of increasing blade count. However, in the total noise, the tonal peak at the first harmonics of BPF remains unchanged between the two cases. Hence, the OASPL on the hemisphere concentrates more around the propeller plane and the maximum noise level remains the same (see Fig. 12c). Interestingly, one would expect a reduction in the tonal noise for Case 3 as a result of increasing number of blades that decrease the loading per blade and, as a consequence, the loading noise component.

However, this is not observed in the total noise, in particular for the first two harmonics of BPF. In order to investigate this aspect, the development of thickness and loading noise contributions under varying *J* and blade counts are displayed in Fig. 16. When the value of *J* decreases both thickness and loading noise are increased, hence the total noise increases. It is noted that, compared to the loading noise, the thickness noise dominates when the value of *J* decreases. When comparing Case 2 against Case 3, the loading noise decreases as a result of increasing blade numbers. However, due to the lower *J*, and the addition of extra thickness noise source due to the addition of extra blades, the thickness noise still dominates the total noise radiated to the far-field. As a consequence, the reduction in the loading noise is overshadowed by the dominance of the thickness noise, thus, the total noise at the first harmonic of BPF remains unchanged. The results highlight the importance of thickness noise in the propeller noise predictions, in particular, for large propellers with many blades operating at relatively lower *J*.

The noise signatures at prescribed ground microphone locations are computed for Case 2 and Case 3. At Mic 1, the noise signature shows a similar trend for both cases. Conversely, at Mic 2, the two cases display opposite interference patterns. This is attributed to the variation in the source directivity on the noise hemisphere and the ground reflection. As expected, at Mic 1, the maximum OASPL remains the same (see Fig. 14a). However, it is increased by 3.5 dBA in A-weighted OASPL (see Fig. 14b). This is
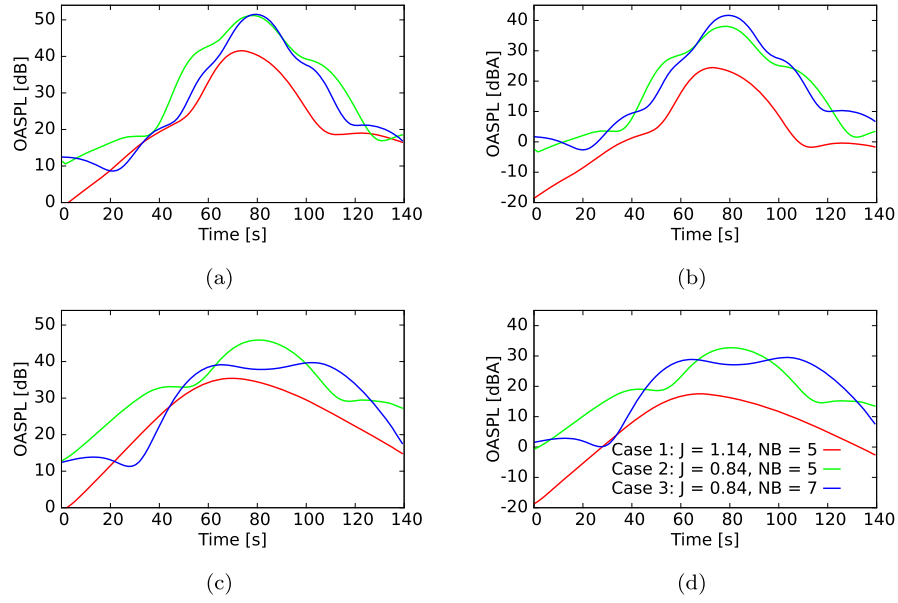
Fig. 14. On-ground noise levels at microphone 1 in dB (a), dBA (b) and microphone 2 in dB (c), dBA (d) as a function of flight mission time.
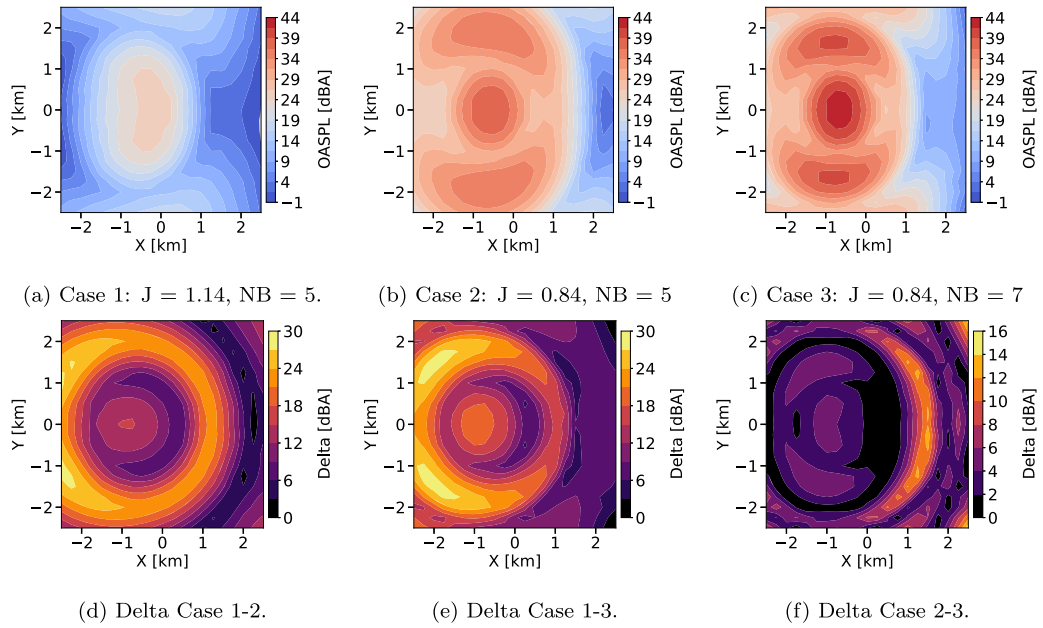
Fig. 15. Noise footprints at flyover time 70 s and the field difference between them for the test cases under consideration.
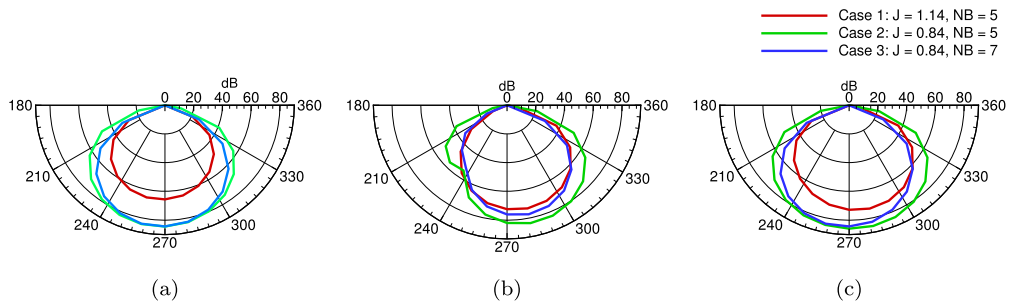
Fig. 16. Comparison of the source noise levels at the first harmonic of BPF on the xz-plane for thickness noise (a), loading noise (b), and total noise (c).

due to the frequency dependence of the A-weighted noise metric. Magliozzi et al. [38] also highlighted this aspect and stated that adding blades raises the frequencies generated, so that metrics such as A-weighted OASPl commonly used in aircraft community noise assessments may increase with increased blade count. At Mic 2, the maximum A-weighted OASPL is decreased by 4 dBA. The noise footprints at flyover time 70 s are computed for Case 2 and Case 3. The noise levels are relatively insensitive to the change in the number of blades except the interference pattern that narrows towards the center of the ground area. The increase in the blade count from 5 to 7 contributes to a mismatch up to 16 dBA on the acoustic footprint that is mainly distributed around the right edge of the ground area.

5. Conclusion

A new computational framework that couples computationally efficient methods, which were initially validated against high-fidelity simulation results, is presented to predict the noise footprint of a propeller. The outlined approach showed good agreement with the reference data in terms of aerodynamic and aeroacoustic predictions from source noise prediction to noise footprint simulation. In addition, the tonal noise predicted with the frequency-domain formulation demonstrated fairly good agreement with both high-fidelity and time-domain compact dipole/monopole predictions that confirm the reliability and computational efficiency of the frequency-domain formulation for propeller tonal noise predictions. The computational framework is then applied to explore the correlation between propeller parameters, i.e., advance ratio and blade count, and the noise footprints. It is found that for a given thrust, a drop in advance ratio can alter the source directivity dramatically, resulting in a variation up to 30 dBA on the acoustic footprint. When the advance ratio is kept the same, and the number of blades increases from 5 to 7, the variation becomes 16 dBA due to the change in the source directivity, but the maximum noise level remains the same. The latter condition reduces each blade's loading and, consequently, the associated noise. However, the total noise remains unchanged as a consequence of increasing thickness noise due to the lower advance ratio, high blade tip Mach number, and addition of extra blades.

The results suggest that the on-ground noise levels are more sensitive to the variation in the advance ratio than the blade count. In general, on-ground noise levels can be reduced significantly by increasing the advance ratio without penalizing the propeller aerodynamic performance. The on-ground noise levels can also be reduced considerably by increasing the blade count only if the tonal noise at higher harmonics is targeted.

This paper represents an initial investigation into the efficient prediction of propeller noise emission and footprint. A more comprehensive analysis evaluating the impact of unsteady loading, i.e., propeller at an angle of attack, varying weather conditions, and ground effects, must be included for more realistic scenarios. Future studies will also examine other effects, such as atmospheric turbulence, multiple reflections, and diffraction from complex urban geometries.

Declaration of competing interest

The authors declare that they have no known competing financial interests or personal relationships that could have appeared to influence the work reported in this paper.

Acknowledgements

References

[1] R. Guski, D. Schreckenberg, R. Schuemer, WHO environmental noise guidelines for the European region: a systematic review on environmental noise and annoyance, Int. J. Environ. Res. Public Health 14 (12) (2017) 1539.

[2] M. Basner, S. McGuire, WHO environmental noise guidelines for the European region: a systematic review on environmental noise and effects on sleep, Int. J. Environ. Res. Public Health 15 (3) (2018) 519.

[3] A.-M. Nassur, M. Lefèvre, B. Laumon, D. Léger, A.-S. Evrard, Aircraft noise exposure and subjective sleep quality: the results of the debats study in France, Behav. Sleep Med. 17 (4) (2019) 502–513.

[4] E. Van Kempen, M. Casas, G. Pershagen, M. Foraster, WHO environmental noise guidelines for the European region: a systematic review on environmental noise and cardiovascular and metabolic effects: a summary, Int. J. Environ. Res. Public Health 15 (2) (2018) 379.

[5] A.-S. Evrard, L. Bouaoun, P. Champelovier, J. Lambert, B. Laumon, Does exposure to aircraft noise increase the mortality from cardiovascular disease in the population living in the vicinity of airports? Results of an ecological study in France, Noise & Health 17 (78) (2015) 328.

[6] H.D. Kim, A. Perry, P. Ansell, A Review of Distributed Electric Propulsion Concepts for Air Vehicle Technology, 2018.

[7] ECAC, ECAC.CEAC Doc. 29, Report on standard method of computing noise contours around civil airports, vol. 2: Technical guide, Tech. Rep., European Civil Aviation Conference (ECAC), 2016.

[8] D. Casalino, W.C. van der Velden, G. Romani, Community noise of urban air transportation vehicles, in: AIAA Scitech 2019 Forum, 2019, p. 1834.

[9] Z. Jia, S. Lee, Acoustic analysis of urban air mobility quadrotor aircraft, in: Vertical Flight Society (VFS) Aeromechanics for Advanced Vertical Flight Technical Meeting, 2020.

[10] Y. Fuerkaiti, D. Casalino, F. Avallone, D. Ragni, Toward inclusion of atmospheric effects in the aircraft community noise predictions, J. Acoust. Soc. Am. 150 (2) (2021) 759–768.

[11] W. van der Velden, G. Romani, D. Casalino, Validation and insight of a full-scale s-76 helicopter rotor using the lattice-Boltzmann method, Aerosp. Sci. Technol. 118 (2021) 107007.

[12] C. Teruna, D. Ragni, F. Avallone, D. Casalino, A rod-linear cascade model for emulating rotor-stator interaction noise in turbofans: a numerical study, Aerosp. Sci. Technol. 90 (2019) 275–288.

[13] G. Romani, Q. Ye, F. Avallone, D. Ragni, D. Casalino, Numerical analysis of fan noise for the nova boundary-layer ingestion configuration, Aerosp. Sci. Technol. 96 (2020) 105532.

[14] G. Romani, E. Grande, F. Avallone, D. Ragni, D. Casalino, Performance and noise prediction of low-Reynolds number propellers using the lattice-Boltzmann method, Aerosp. Sci. Technol. (2021) 107086.

[15] D. Casalino, M. Barbarino, A. Visingardi, Simulation of helicopter community noise in a realistic urban environment, https://doi.org/10.2514/6.2010-4004, 2010.

[16] D. Casalino, W.C. van der Velden, G. Romani, I. Gonzalez-Martino, Aeroacoustic analysis of urban air operations using the lb/vles method, in: 25th AIAA/CEAS Aeroacoustics Conference, 2019, p. 2662.

[17] G. Romani, D. Casalino, Rotorcraft blade-vortex interaction noise prediction using the lattice-Boltzmann method, Aerosp. Sci. Technol. 88 (2019) 147–157.

[18] R.J. Higgins, G.N. Barakos, S. Shahpar, I. Tristanto, A computational fluid dynamic acoustic investigation of a tiltwing evtol concept aircraft, Aerosp. Sci. Technol. 111 (2021) 106571.

[19] C. Nana, J.-M. Moschetta, E. Bénard, S. Prothin, T. Jardin, Experimental and numerical analysis of quiet mav rotors, in: 50th 3AF International Conference on Applied Aerodynamics, 2015.

[20] N.S. Zawodny, D.D. Boyd Jr., C.L. Burley, Acoustic characterization and prediction of representative, small-scale rotary-wing unmanned aircraft system components, in: Proceedings of 72nd American Helicopter Society International Annual Forum, 2016.

[21] R. Serré, N. Gourdain, T. Jardin, A. Sabaté López, V. Sujjur Balaramraja, S. Belliot, M.C. Jacob, J.-M. Moschetta, Aerodynamic and acoustic analysis of an optimized low Reynolds number rotor, in: International Symposium on Transport Phenomena and Dynamics of Rotating Machinery, 2017.

[22] K. Pascioni, S.A. Rizzi, Tonal noise prediction of a distributed propulsion unmanned aerial vehicle, in: 2018 AIAA/CEAS Aeroacoustics Conference, 2018, p. 2951.

[23] S. Rizzi, D. Huff, D. Boyd, P. Bent, B. Henderson, K. Pascioni, C. Sargent, D. Josephson, M. Marsen, H. He, et al., Urban air mobility noise: Current practice, gaps, and recommendations, Tech. Rep., NASA TP-2020-5007433, 2020.

[24] H. Bian, Q. Tan, S. Zhong, X. Zhang, Assessment of uam and drone noise impact on the environment based on virtual flights, Aerosp. Sci. Technol. 118 (2021) 106996.

[25] D.B. Hanson, D.J. Parzych, Theory for noise of propellers in angular inflow with parametric studies and experimental verification, Final Report United Technologies Corporation, 1993.

[26] M.T. Kotwicz Herniczek, D. Feszty, S.-A. Meslioui, J. Park, F. Nitzsche, Evaluation of acoustic frequency methods for the prediction of propeller noise, AIAA J. 57 (6) (2019) 2465–2478.

[27] D.B. Hanson, Helicoidal surface theory for harmonic noise of propellers in the far field, AIAA J. 18 (10) (1980) 1213–1220.

[28] D. Casalino, E. Grande, G. Romani, D. Ragni, F. Avallone, Definition of a benchmark for low Reynolds number propeller aeroacoustics, Aerosp. Sci. Technol. 113 (2021) 106707.

[29] C. Poggi, M. Rossetti, G. Bernardini, U. Iemma, C. Andolfi, C. Milano, M. Gennaretti, Surrogate models for predicting noise emission and aerodynamic performance of propellers, Aerosp. Sci. Technol. (2021) 107016.

[30] Z. Zhang, Y. Lin, Data-driven seismic waveform inversion: a study on the robustness and generalization, IEEE Trans. Geosci. Remote Sens. 58 (10) (2020) 6900–6913.

[31] B. Moseley, T. Nissen-Meyer, A. Markham, Deep learning for fast simulation of seismic waves in complex media, Solid Earth 11 (4) (2020) 1527–1549.

[32] M. Drela, M. Giles, Viscous-inviscid analysis of transonic and low Reynolds number airfoils, AIAA J. 25 (1987) 1347–1355, https://doi.org/10.2514/3.9789.

[33] J.E.F. Williams, D.L. Hawkings, Sound generation by turbulence and surfaces in arbitrary motion, Philos. Trans. R. Soc. Lond. 264 (1151) (1969) 321–342.

[34] D. Casalino, An advanced time approach for acoustic analogy predictions, J. Sound Vib. 261 (4) (2003) 583–612.

[35] F. Farassat, G.P. Succi, The prediction of helicopter discrete frequency noise, Vertica 7 (4) (1983) 309–320.

[36] T. Zhou, H. Jiang, Y. Sun, R.J. Fattah, X. Zhang, B. Huang, L. Cheng, Acoustic characteristics of a quad-copter under realistic flight conditions, in: 25th AIAA/CEAS Aeroacoustics Conference, 2019, p. 2587.

[37] Y. Yang, Y. Liu, Y. Li, E. Arcondoulis, Y. Wang, Aerodynamic and aeroacoustic performance of an isolated multicopter rotor during forward flight, AIAA J. 58 (3) (2020) 1171–1181.

[38] B. Magliozzi, D. Hanson, R. Amiet, Propeller and propfan noise, in: Aeroacoustics of Flight Vehicles: Theory and Practice, vol. 1, 1991, pp. 1–64.